POLYOXOMETALATES

Open Access
RESEARCH ARTICLE

Atomically precise M_{15} (M = Au/Ag/Cu) alloy nanoclusters: Structural analysis, optical and electrocatalytic CO_2 reduction properties

Along Ma[§], Jiawei Wang[§], Yifei Wang, Yang Zuo, Yonggang Ren, Xiaoshuang Ma ✉, and Shuxin Wang ✉

College of Materials Science and Engineering, Qingdao University of Science and Technology, Qingdao 266042, China
[§]Along Ma and Jiawei Wang contributed equally to this work.

Cite This: *Polyoxometalates*, **2024**, *3*, 9140054

Read Online

ABSTRACT: Herein, the overall structure of a nanocluster coprotected by phosphine and mercaptan ligands **[Au_7Ag_8(SPh)$_6$((*p*-OMePh)$_3$P)$_8$]NO_3** (**Au_7Ag_8**) was reported. For comparison, a previously reported nanocluster with the same structure, but a different metal composition, **[$Au_{13}Cu_2$(TBBT)$_6$((*p*-ClPh)$_3$P)$_8$]SbF_6** (**$Au_{13}Cu_2$**), was synthesized. In addition, their optical and electrocatalytic CO_2 reduction properties were comprehensively compared. The results reveal that the photoluminescence quantum yield (PLQY) of the Ag-doped **Au_7Ag_8** nanocluster is 1.62%, which is seven times greater than that of the Cu-doped **$Au_{13}Cu_2$** nanocluster (PLQY = 0.23%). Furthermore, the **$Au_{13}Cu_2$** nanocluster demonstrates significantly enhanced catalytic selectivity for CO, with a CO Faradaic efficiency ranging from 79.7% to 90.4%, compared with that of the **Au_7Ag_8** nanocluster (CO Faradaic efficiency: 67.2%–77.7%) within a potential range of 0.5 to −1.1 V. From structural analyses, the superior CO selectivity of **$Au_{13}Cu_2$** is attributed to the copper dopant.

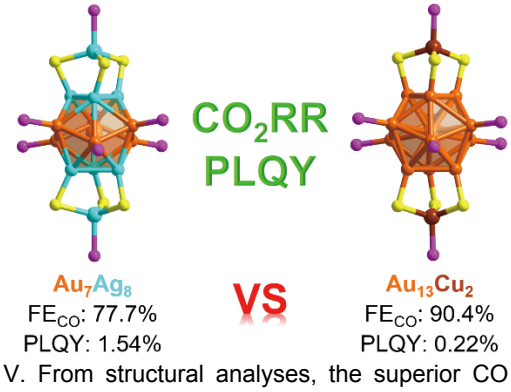

KEYWORDS: alloy nanocluster, photoluminescence, electrocatalytic CO_2 reduction reaction (eCO_2RR)

1 Introduction

Ligand-protected atomically precise metal nanoclusters have attracted significant attention because of their definite atomic structures and exceptional physical and chemical properties, which encompass attributes such as luminescence, chirality, electrochemistry, and catalysis [1–25]. Within the realm of metal nanoclusters, those sharing similar structures but comprising different metals offer a unique opportunity for the in-depth exploration of atomic level metal synergy [26–31]. To completely harness their potential in various applications, synthesizing alloy nanoclusters with analogous structures but distinct metal compositions is crucial, enabling a comprehensive examination of the factors influencing their properties. Although substantial progress has been made in the preparation of alloy nanoclusters with similar structures, their limited availability continues to hinder their widespread application [32–37]. Consequently, the synthesis of analogous alloy nanoclusters is imperative.

Research on such alloy nanoclusters has attracted increasing attention in previous studies [11, 20, 28, 31, 33, 38–41]. From these studies, a preliminary understanding of the origin of the optical properties of metal nanoclusters is obtained, and theoretical guidance for designing nanoclusters with high photoluminescence quantum yields (PLQYs) is provided [4, 40, 42, 43]. For example, the luminescence of metal nanoclusters primarily originates from their metal cores, and the free electron shrinkage induced by doping with inert metals can significantly increase the PLQY of nanoclusters [26]. On the other hand, as an ideal model catalyst, metal nanoclusters can be used to adjust the species and selectivity of products obtained by the electrocatalytic CO_2 reduction reaction (eCO_2RR) and further investigate the catalytic reaction mechanism at the atomic level [44–47]. For instance, when Cd doped on the Au nanocluster surface can help capture CO_2, the hydrogen evolution reaction was effectively restrained [44]. In addition, doping gold atoms into the core of nanoclusters can cause the centralization of free valence electrons towards the core, which is beneficial for eCO_2RR [8]. Metal catalysts are crucial in electrocatalysis [48–50]. Recently, studies on the catalytic performance of isomeric alloy nanoclusters have also gained attention [8, 11]. Research into catalytic properties based on precise structures demonstrates promise for guiding the design and synthesis of alloy catalysts with high catalytic activity.

Herein, the synthesis, crystal structure analysis, and optical and electrocatalytic CO_2 reduction properties of **[Au_7Ag_8(SPh)$_6$((*p*-OMePh)$_3$P)$_8$]NO_3** (**Au_7Ag_8**) nanoclusters were reported. Meanwhile, the **[$Au_{13}Cu_2$(TBBT)$_6$((*p*-ClPh)$_3$P)$_8$]SbF_6** (**$Au_{13}Cu_2$**)

Received: November 2, 2023; **Revised:** December 11, 2023
Accepted: January 7, 2024

✉Address correspondence to Shuxin Wang, shuxin_wang@qust.edu.cn; Xiaoshuang Ma, xiaoshuang_ma@qust.edu.cn

nanocluster was also synthesized for comparison [33]. Both nanoclusters exhibit the same core structure, but differ in their metallic compositions. The PLQY of 1.62% for **Au_7Ag_8** is considerably greater than that for **$Au_{13}Cu_2$** (0.23%). In addition, the two catalysts exhibit different catalytic properties toward eCO_2RR. **$Au_{13}Cu_2$** exhibits a high CO Faradaic efficiency (FE_{CO}) of 90.4% at −0.6 V, which is considerably greater than that of the **Au_7Ag_8** nanocluster (FE_{CO}: 77.7% at −0.6 V). Understandably, Cu doping can increase the selectivity for reducing CO_2 to the CO product. Our work can aid in obtaining a better understanding of the effect of metal synergy on optical and catalytic properties at the atomic level.

2 Experimental section

2.1 Chemicals

Silver nitrate ($AgNO_3$, 98% metal basis), hydrogen tetrachloroaurate tetrahydrate ($HAuCl_4{\cdot}4H_2O$, 99.5% metal basis), copper chloride dihydrate ($CuCl_2{\cdot}2H_2O$, 99.9%, metal basis), tris(4-methoxyphenyl) phosphine ($(p\text{-}OMePh)_3P$, 98%), tris(4-chlorophenyl)phosphine ($(p\text{-}ClPh)_3P$, 99.5%), thiophenol (C_6H_6S, PhSH, 98%), 4-tert-butylthiophenol ($C_{10}H_{14}S$, TBBT, 98%), sodium hexafluoroantimonate ($NaSbF_6$, 99%), sodium borohydride ($NaBH_4$, 99.9%), methylene chloride (CH_2Cl_2, HPLC grade), diethyl ether ($C_2H_5OC_2H_5$, HPLC grade), methanol (CH_3OH, HPLC grade), acetonitrile (CH_3CN, HPLC grade), n-hexane (C_6H_{14}, HPLC grade), ethyl alcohol (CH_3CH_2OH, HPLC grade), acetone (C_3H_6O, HPLC grade), and isopropanol (C_3H_8O) were commercial and used directly.

2.2 Synthesis of the Au_7Ag_8 nanocluster

Typically, $HAuCl_4{\cdot}4H_2O$ (0.20 g/mL, 300 μL, 0.15 mmol) and $AgNO_3$ (90 mg, 0.53 mmol, dissolved in 2 mL of H_2O) were injected into 5 mL of ethyl alcohol and 15 mL of CH_2Cl_2 under intense agitation. After stirring for 5 min, $(p\text{-}OMePh)_3P$ (160 mg, 0.45 mmol) and PhSH (0.24 mL, 2.34 mmol) were successively added to the reaction mixture, and the solution color changed from brown to light-yellow. After vigorous stirring for 0.5 h, $NaBH_4$ (90 mg, 2.38 mmol, dissolved in 5 mL of H_2O) was rapidly added to the reaction solution, and the reaction solution gradually turned dark. The entire reaction lasted for 12 h at ~ 25°C; finally, the **Au_7Ag_8** nanocluster was produced (yield ~ 25%, Au atom basis). Next, to obtain the pure product of **Au_7Ag_8** nanoclusters, the reaction solution was centrifuged and evaporated. The crude product of **Au_7Ag_8** nanoclusters was washed thrice with CH_3OH (10 mL) and n-hexane (10 mL), affording pure **Au_7Ag_8** nanoclusters. Black and block-shaped crystals were obtained by crystallizing pure **Au_7Ag_8** nanoclusters in $CH_2Cl_2/C_2H_5OC_2H_5$ (1:3) after ~ 4 days at room temperature.

2.3 Synthesis of the $Au_{13}Cu_2$ nanocluster

$Au_{13}Cu_2$ was synthesized according to a previously reported method with slight modifications [33]. First, $HAuCl_4{\cdot}4H_2O$ (0.2 g/mL, 400 μL, 0.2 mmol) and $CuCl_2{\cdot}2H_2O$ (40 mg, 0.23 mmol) were successively added to a mixed solution of 5 mL of CH_3OH and 15 mL of CH_2Cl_2. After 3 min, $(p\text{-}ClPh)_3P$ (300 mg, 0.82 mmol) was added. The solution color changed from orange to green after 20 min. Then, TBBT (100 μL, 0.6 mmol) was injected into the reaction solution. After 20 min, the reaction solution became muddy-white. Finally, $NaBH_4$ (80 mg, 2.1 mmol, dissolved in 5 mL of H_2O) was rapidly added to the reaction mixture. After 12 h, $NaSbF_6$ (0.2 mmol, 50 mg, dissolved in 1 mL of CH_3OH) was added to the organic phase, and the reaction solution was dried. Next, the crude product of **$Au_{13}Cu_2$** nanoclusters was washed thrice with CH_3OH and CH_3CN, and the crude product was extracted with acetone. By the liquid diffusion of C_6H_{14} into the CH_2Cl_2 solution of the nanocluster for 3 days, black crystals were obtained.

3 Results and discussion

3.1 Preparation and characterization of the Au_7Ag_8 nanocluster

The **Au_7Ag_8** nanocluster was prepared using the one-pot method. Briefly, Au–Ag complexes (Au(I)/Ag(I)-SR/PR_3, SR = SPh; PR_3 = $(p\text{-}OMePh)_3P$) were reduced by $NaBH_4$ in a mixed solvent (CH_2Cl_2 and CH_3OH), and the reaction was allowed to proceed for 12 h. By diffusing $C_2H_5OC_2H_5$ into the CH_2Cl_2 solution of the coarse product, black block-shaped crystals were obtained (Fig. S1 in the Electronic Supplementary (ESM)). A detailed synthetic procedure can be found in the experimental section.

Single-crystal X-ray diffraction (SC-XRD) revealed that the structure and exact molecular formula of the nanocluster was **$Au_7Ag_8(SPh)_6((p\text{-}OMePh)_3P)_8$** (Fig. 1(a)). The molecular composition and valence state of **Au_7Ag_8** were confirmed by electrospray ionization mass spectrometry (ESI-MS, in the positive mode). As shown in Fig. 1(b), a distinct peak labeled B with an m/z value of 5715.17 Da was observed, corresponding to the +1 valence state (m/z = 1) of **$Au_7Ag_8(SPh)_6((p\text{-}OMePh)_3P)_8$**. The experimental results were in good agreement with the theoretical value (calculated to be 5715.06 Da, with a deviation of 0.11). Peaks A and C were attributed to the formulas $[Au_6Ag_9(SPh)_6((p\text{-}OMePh)_3P)_8]^+$ and $[Au_8Ag_7(SPh)_6((p\text{-}OMePh)_3P)_8]^+$, respectively. The above data indicate that both nanoclusters exhibit an 8-electron structure (15 − 6 − 1 = 8). Furthermore, X-ray photoelectron spectroscopy (XPS) measurements confirmed the presence of Au, Ag, S, P, O, N, and C in the **Au_7Ag_8** crystals (Fig. 1(c)). The Au/Ag atomic ratio in **Au_7Ag_8** was estimated to be 6.87/7.13, which was in agreement with the SC-XRD result (7/8) (Fig. S2 in the ESM). The elemental composition (Au, Cu, S, P, C, and Cl) of the **$Au_{13}Cu_2$** nanocluster was also confirmed (Fig. S3 in the ESM). In addition, thermogravimetric analysis (TGA) confirmed the metal-to-ligand ratio in **Au_7Ag_8**, and the experimental value of 60.63% was in agreement with the theoretical value of 61.20% (Fig. 1(d)). Moreover, energy-dispersive spectrometry confirmed the presence of Au, Ag, S, P, and O in the **Au_7Ag_8** crystals (Fig. S4 in the ESM). In the XPS spectrum, the presence of the N peak and absence of the Cl peak indicated that the anionic component of the cluster was NO_3^- and not Cl^-.

3.2 Crystal structure of the two M_{15} nanoclusters

The crystal structures of the **Au_7Ag_8** and **$Au_{13}Cu_2$** nanoclusters were compared [33]. The comprehensive structure of the **Au_7Ag_8** nanocluster was elucidated by SC-XRD (Fig. S5(a) in the ESM). Remarkably, the structure of the **Au_7Ag_8** nanocluster was fundamentally identical to that of the **$Au_{13}Cu_2$** nanocluster (Fig. S5(b) in the ESM). To compare the structural differences, the crystal structures of the **Au_7Ag_8** and **$Au_{13}Cu_2$** nanoclusters are shown in Fig. 2. The **Au_7Ag_8** nanocluster comprised an icosahedral

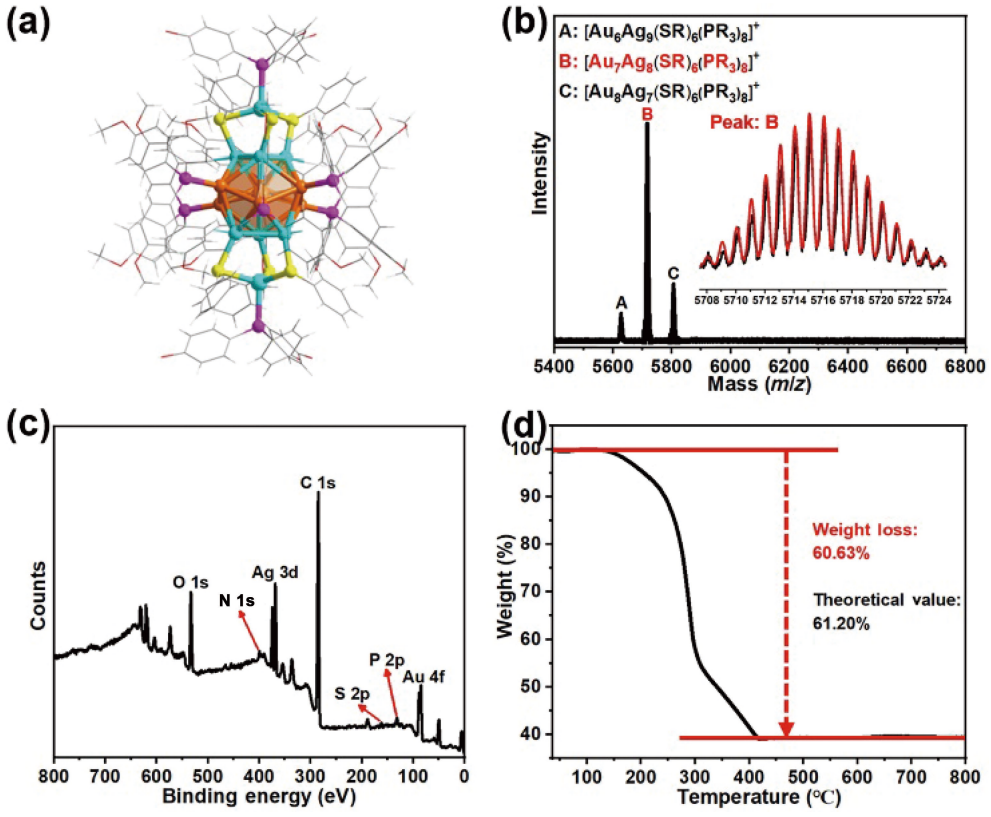

Figure 1 (a) Overall structure of the $\mathbf{Au_7Ag_8}$ nanocluster. (b) ESI-MS profile of $\mathbf{Au_7Ag_8}$ in the positive mode. Inset: comparison of the calculated (red) and experimental (black) isotope distribution of $[Au_7Ag_8(SPh)_6((p\text{-}OMePh)_3P)_8]^+$. (c) XPS spectrum of the $\mathbf{Au_7Ag_8}$ nanocluster. (d) TGA curve of the $\mathbf{Au_7Ag_8}$ nanocluster. Color labels: orange = Au; light blue = Ag; magenta = P; red = O; yellow = S; gray = C; white = H.

Au_7Ag_6 metal core surrounded by two $Ag(SR)_3PR_3$ surface motifs at the top and bottom, forming the $Au_7Ag_8(SR)_6(PR_3)_2$ structure (Fig. 2(a) and 2(b)). Each of the six Au atoms on the Au_7Ag_6 kernel surface was bonded to a PR_3 ligand, resulting in the overall structure of $\mathbf{Au_7Ag_8(SR)_6(PR_3)_8}$ (Fig. 2(c) and 2(d)). For the $\mathbf{Au_{13}Cu_2}$ nanocluster, the M_{13} core was entirely composed of gold, with copper positioned at the bottom and top of the icosahedron, forming the overall structure of $\mathbf{Au_{13}Cu_2(SR')_6(PR'_3)_8}$ (SR' = $C_{10}H_{13}S$; PR'_3 = (p-ClPh)$_3$P). A detailed analysis of the bond lengths is shown in Fig. S6 in the ESM. In the case of the M_{13} metal core, the average Au_{kernel}–$Au/Ag_{icosahedral}$ surface bond length for $\mathbf{Au_7Ag_8}$ (2.776 Å) was similar to that of $\mathbf{Au_{13}Cu_2}$ (2.772 Å). Furthermore, the $Au/Ag_{icosahedral\ surface}$–$Au/Ag_{icosahedral\ surface}$ bond lengths for $\mathbf{Au_7Ag_8}$ (2.915 Å) and $\mathbf{Au_{13}Cu_2}$ (2.916 Å) were nearly identical. Because the atomic radius of Cu was less than that of Ag, significant differences existed in the distances between S and the metal atoms at both ends. In $\mathbf{Au_7Ag_8}$, the average bond length between S and the two Ag atoms was 2.609 Å, whereas in $\mathbf{Au_{13}Cu_2}$, the bond length between S and the two copper atoms was 2.396 Å. The atomic radius not only affected the bonding distances with the thiol ligands but also significantly affected the P–metal distances. For instance, in the $\mathbf{Au_7Ag_8}$ nanocluster, the distance between P and the terminal Ag atoms was 2.562 Å, which was notably greater than that of the P–Cu distance in $\mathbf{Au_{13}Cu_2}$ (2.297 Å). Simultaneously, owing to the relatively small difference in the atomic radii between Au and Ag, the distance between S/P and the M_{13} core was relatively minor (see Fig. S6 in the ESM for details).

Next, the molecular packing arrangements were further analyzed. As shown in Fig. S7 in the ESM, $\mathbf{Au_7Ag_8}$ crystallized in the $P\bar{3}1c$ space group within the trigonal crystal system (Table S1 in the ESM summarizes the detailed crystal parameters). In contrast, $\mathbf{Au_{13}Cu_2}$ crystallized in the $P21/c$ space group within the monoclinic crystal system. Furthermore, $\mathbf{Au_7Ag_8}$ clusters were arranged in the unit cells in the "ABAB" packing mode (Fig. S8 in the ESM). This packing mode was consistent with those of several nanoclusters but differed from the "ABBA" packing mode observed for the $\mathbf{Au_{13}Cu_2}$ nanocluster (Fig. S9 in the ESM) [40, 51].

3.3 Optical properties of the two M_{15} nanoclusters

As shown in Fig. 3, the optical properties of the $\mathbf{Au_7Ag_8}$ and $\mathbf{Au_{13}Cu_2}$ nanoclusters were comparatively analyzed. For $\mathbf{Au_7Ag_8}$, the ultraviolet–visible (UV–vis) absorption spectrum revealed four prominent absorption peaks at approximately 348, 386, 460, and 643 nm, respectively, in addition to one less intense peak at 500 nm (Fig. 3(a)). In CH_2Cl_2, the solution appeared yellow.

After converting the UV–vis absorption spectra into photoelectron spectra, the excitation energies of the $\mathbf{Au_7Ag_8}$ nanocluster were 1.93, 2.48, 2.69, 3.21, and 3.56 eV, respectively (Fig. 3(c)). The experimental energy gap was calculated to be 1.66 eV. In contrast, for $\mathbf{Au_{13}Cu_2}$, two intense absorption peaks were observed at 383 and 573 nm, in addition to a weaker peak at 752 nm (Fig. 3(b)). In CH_2Cl_2, the solution appeared yellow-green. Photoelectron spectra revealed that the excitation energies of the $\mathbf{Au_{13}Cu_2}$ nanocluster were 1.65, 2.16, and 3.24 eV, respectively, and the experimental energy gap was calculated to be 1.29 eV (Fig. 3(c) above). Moreover, the photoluminescence (PL) spectra of $\mathbf{Au_7Ag_8}$ and $\mathbf{Au_{13}Cu_2}$ nanoclusters were compared with that of $Ag_{25}(SPhMe_2)_{18}$ (PLQY = 0.6%, CH_2Cl_2) as a reference (Fig. 3(d))

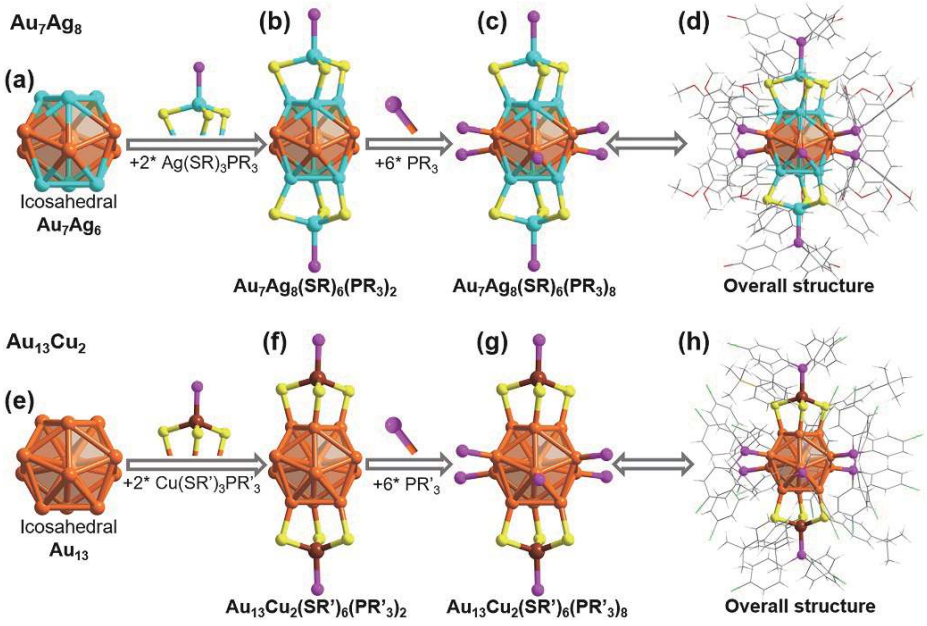

Figure 2 Structural analysis of the Au_7Ag_8 and $Au_{13}Cu_2$ nanoclusters. (a) Icosahedral Au_7Ag_6 kernel. (b) $Au_7Ag_8(SR)_6(PR_3)_2$ structure with two $Ag(SR)_3PR_3$ surface motif structures at the top and bottom, respectively. (c) $Au_7Ag_8(SR)_6(PR_3)_8$ structure with six waist PR_3 ligands. (d) Overall structure of the Au_7Ag_8 nanocluster. (e) Icosahedral Au_{13} kernel. (f) $Au_{13}Cu_2(SR')_6(PR'_3)_2$ structure with two $Cu(SR')_2PR'_3$ surface motif structures at the top and bottom, respectively. (g) $Au_{13}Cu_2(SR')_6(PR'_3)_8$ structure with six waist PR'_3 ligands. (h) Overall structure of the $Au_{13}Cu_2$ nanocluster. Color labels: orange = Au; light blue = Ag; brown = Cu; yellow = S; magenta = P; gray = C; green = Cl; white = H.

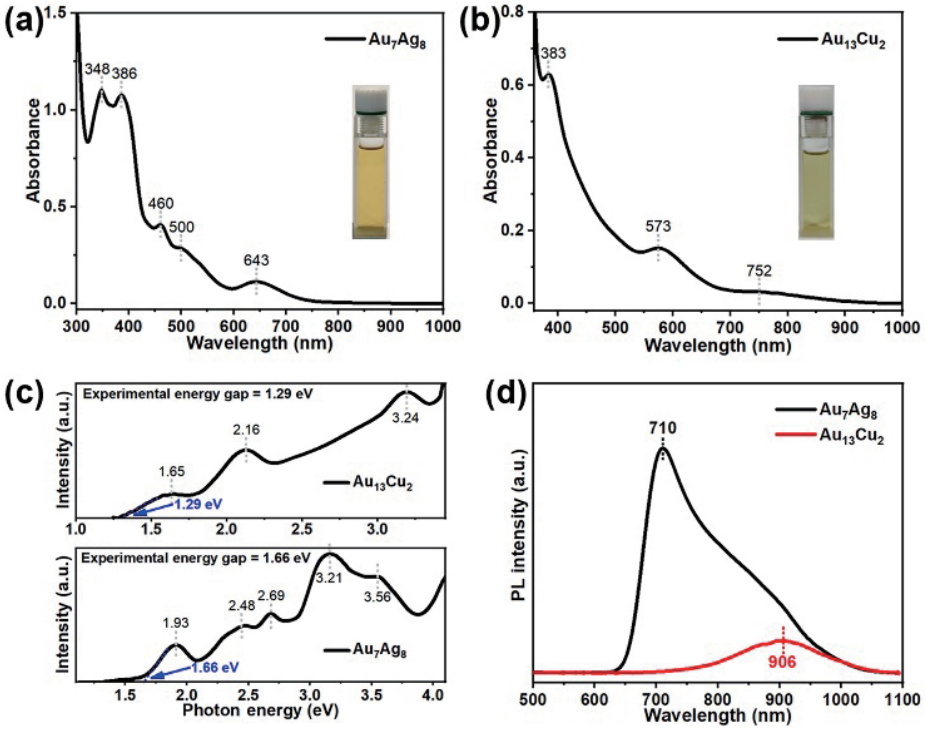

Figure 3 Optical properties of Au_7Ag_8 and $Au_{13}Cu_2$ nanoclusters. (a) and (b) UV–vis absorbance spectra of Au_7Ag_8 and $Au_{13}Cu_2$ in CH_2Cl_2. Insets show photographs of the two nanoclusters in CH_2Cl_2. (c) Photoelectron spectra plotted along the energy axis of Au_7Ag_8 (under) and $Au_{13}Cu_2$ (upper). (d) Photoluminescence spectra of Au_7Ag_8 and $Au_{13}Cu_2$ in CH_2Cl_2.

[20]. Au_7Ag_8 and $Au_{13}Cu_2$ exhibited distinct PL properties. In CH_2Cl_2, Au_7Ag_8 exhibited a prominent emission peak at 710 nm with a PLQY of 1.62%. Conversely, $Au_{13}Cu_2$ exhibited a significantly lower PLQY (0.23%), and its emission band was red-shifted to 906 nm. In the solid state, the emission peak exhibited a similar red-shift from 813 nm for Au_7Ag_8 to 947 nm for $Au_{13}Cu_2$ (Fig. S10 in the ESM).

3.4 Electrocatalytic CO_2 reduction properties of the two M_{15} nanoclusters

To investigate the electrocatalytic CO_2 reduction properties of the

two M_{15} nanoclusters, electrocatalytic CO_2 reduction reactions were conducted in a custom-designed flowcell reactor [52]. Both nanoclusters were deposited onto Ketjen carbon (C) with a loading of 50 wt.%, resulting in the formation of **Au_7Ag_8/C** and **$Au_{13}Cu_2$/C**. Gas chromatography revealed that under all applied potentials (without *IR* correction), CO and H_2 were the only gaseous products. The linear scanning voltammetry curves of **Au_7Ag_8/C** and **$Au_{13}Cu_2$/C** in N_2-saturated (full line) and CO_2-saturated (dashed line) solutions of 1.0 M KOH are shown in Fig. 4(a). The total current densities (j_{Total}) of the two catalysts in the CO_2-saturated electrolyte were considerably greater than those in the N_2-purged electrolyte, respectively, indicating that **Au_7Ag_8/C** and **$Au_{13}Cu_2$/C** can effectively catalyze CO_2RR. Moreover, compared to **Au_7Ag_8/C**, **$Au_{13}Cu_2$/C** exhibited a considerably higher j_{Total} and a more positive onset potential in CO_2/N_2-purged 1.0 M KOH, indicative of a higher CO_2 reduction selectivity. Therefore, the eCO_2RR catalytic activity of **$Au_{13}Cu_2$/C** was greater than that of **Au_7Ag_8/C**, which was attributed to the metal composition of the clusters and not the size of the clusters. As shown in Fig. 4(b), **$Au_{13}Cu_2$/C** exhibited high selectivity for CO under all tested potentials, as confirmed by the higher FE_{CO} of 90.4%, ranging from 59.2% at −1.2 V to 90.4% at −0.6 V (vs. RHE). In contrast, similar to the shape of a volcano, the FE_{CO} of **Au_7Ag_8/C** was measured. The highest FE_{CO} value of 77.7% at −0.6 V (vs. RHE) was obtained, ranging from 61.8% at −1.2 V (vs. RHE) to 77.1% at −0.6 V (vs. RHE). Notably, CO exhibited a higher Faradaic efficiency at positive potentials, and the FE_{CO} of **$Au_{13}Cu_2$/C** was greater than that of **Au_7Ag_8/C** from −0.5 V to −1.1 V (vs. RHE).

The reduction products for the two catalysts were only CO and H_2, and the sum of the FE values was close to 100% under all tested potentials (Fig. 4(d)). Other liquid products were not detected by NMR. Moreover, hydrogen evolution reaction (HER) became dominant at more negative potentials. The highest H_2 Faradaic efficiency (FE_{H2}) reached 37.1% at −1.2 V (vs. RHE) for **Au_7Ag_8/C** and 39.5% at −1.2 V (vs. RHE) for **$Au_{13}Cu_2$/C** (Fig. S11(a) in the ESM). Furthermore, with an increase in the tested potential for the **Au_7Ag_8/C** and **$Au_{13}Cu_2$/C** catalysts, the CO partial current density (j_{CO}) increased (Fig. 4(c)). Compared to **Au_7Ag_8/C, $Au_{13}Cu_2$/C** exhibited a considerably higher CO selectivity under full potentials, which is indicative of the unique advantage of Cu-doped nanoclusters for electrocatalytic reduction of CO_2 to CO. Notably, the H_2 partial current density (j_{H2}) of **$Au_{13}Cu_2$/C** was less than that of **Au_7Ag_8/C** from −0.7 to −1.2 V (vs. RHE), indicating that doping with Cu could increase the selectivity of the CO product at high potentials (Fig. S11(b) in the ESM) [53]. These results indicated that the introduction of a few copper atoms into the nanoclusters can considerably improve the selectivity of CO. Furthermore, the fingerprint absorbance peak (643 nm for **Au_7Ag_8**; 573 nm for **$Au_{13}Cu_2$**) of the two nanoclusters after eCO_2RR was almost the same as before (Fig. S12 in the ESM), indicating that the structure of the two M_{15} nanoclusters essentially maintained.

Furthermore, the electrochemically active surface area (ECSA) of the two M_{15} nanoclusters was estimated. The cyclic voltammetry (CV) curves of **Au_7Ag_8/C** and **$Au_{13}Cu_2$/C** at different scan rates ranging from 0.02 to 0.1 V·s^{-1} were measured (Fig. S13 in the ESM). The double-layer capacitance (C_{dl}) values of the two catalysts were calculated to be 12.43 and 7.02 mF, respectively. Therefore, the ECSA values of **Au_7Ag_8/C** and **$Au_{13}Cu_2$/C** were calculated to be

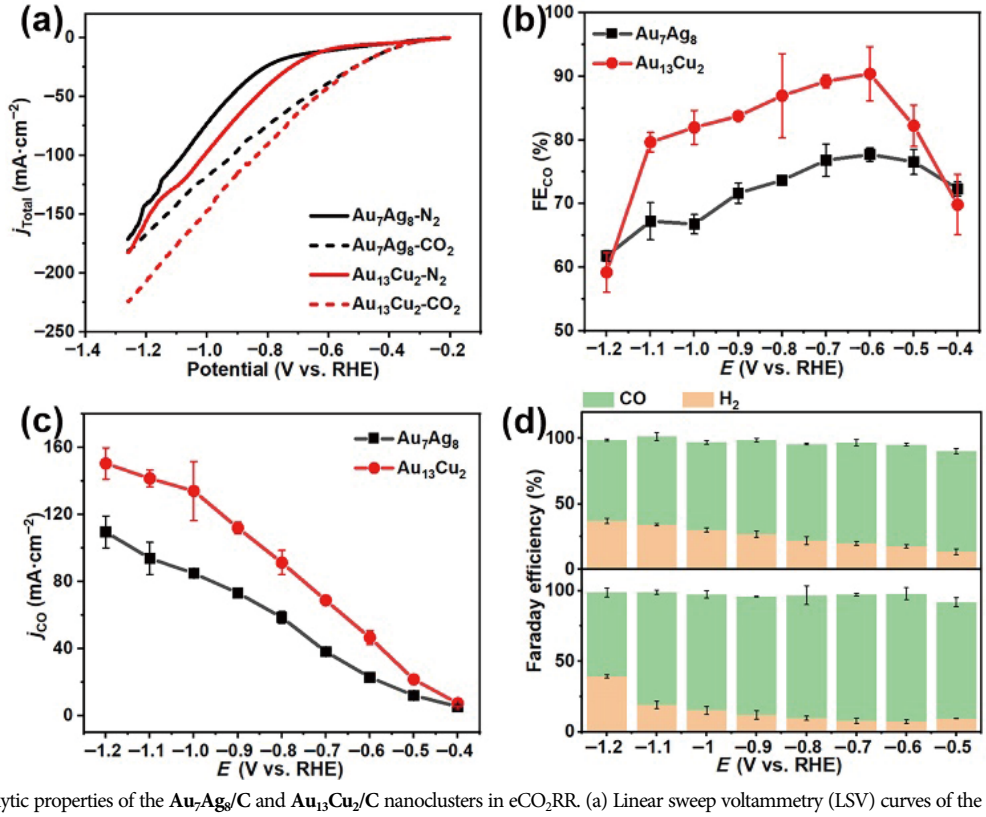

Figure 4 Electrocatalytic properties of the **Au_7Ag_8/C** and **$Au_{13}Cu_2$/C** nanoclusters in eCO_2RR. (a) Linear sweep voltammetry (LSV) curves of the two catalysts in an N_2-purged (full line) and a CO_2-saturated (dashed line) 1.0 M KOH solution. (b) FE_{CO} and (c) j_{CO} of the two catalysts. (d) Total FE for various eCO_2RR products (CO and H_2) of the **Au_7Ag_8/C** (upper) and **$Au_{13}Cu_2$/C** (bottom) catalysts. Error bars represent the standard deviation of three tests at the same applied potential.

310.75 and 175.5 cm^2, respectively.

In contrast, compared with $Au_{13}Cu_2$/C, Au_7Ag_8/C exhibited diminished selectivity for CO; however, the density of active sites in the Au_7Ag_8 nanocluster was significantly greater than that in its $Au_{13}Cu_2$ counterpart. Moreover, to estimate the electron transport capability of Au_7Ag_8/C and $Au_{13}Cu_2$/C, electrochemical impedance spectroscopy (EIS) was performed (Fig. S14 in the ESM). Distinctly different EIS curves were observed, indicating that the two catalysts exhibited different electron transport properties. Compared to $Au_{13}Cu_2$/C, Au_7Ag_8/C exhibited a considerably smaller semicircle diameter; Au_7Ag_8/C exhibited a lower conductivity of interfacial charge-transfer resistance. This result suggested that compared with $Au_{13}Cu_2$, Au_7Ag_8 would provide electrons to the intermediates more efficiently during electroreduction.

4 Conclusions

In summary, Au_7Ag_8 nanocluster was successfully synthesized, and its crystal structure was determined. A previously reported $Au_{13}Cu_2$ nanocluster with a similar isomeric composition was prepared for comparison. The comparison of their optical and catalytic properties revealed that compared with Cu doping, Ag doping effectively enhanced the photoluminescence quantum yield of the nanoclusters (by a factor of 7). In the context of electrocatalytic CO_2 reduction reaction, the addition of a small quantity of copper, while enhancing the catalytic selectivity for CO production, concurrently reduces the ECSA. In an ideal electrocatalyst, a delicate balance between selectivity and preservation of an optimal ECSA should be achieved. Currently, the incorporation of multiple metals to achieve synergistic catalysis for enhanced selectivity and efficiency is underway in our laboratory. Our study provides experimental evidence for understanding and designing nanoclusters with specific properties at the atomic level.

Electronic Supplementary Material: Supplementary material (optical microscopic, SEM-EDS and XPS of Au_7Ag_8; XPS of $Au_{13}Cu_2$; overall structures, bond lengths, unit cells, packing mode of Au_7Ag_8 and $Au_{13}Cu_2$; FE_{H2}, j_{H2}, ECSA, EIS and stability of Au_7Ag_8/C and $Au_{13}Cu_2$/C; crystal structure parameters of Au_7Ag_8) is available in the online version of this article at https://doi.org/10.26599/POM.2024.9140054.

Data availability

All data needed to support the conclusions in the paper are presented in the manuscript and/or the Electronic Supplementary Material. Additional data related to this paper may be requested from the corresponding author upon request.

Acknowledgements

We thank the financial support provided by the National Natural Science Foundation of China (Nos. 22171156 and 21803001), Taishan Scholar Foundation of Shandong Province (China), and Shandong Province Excellent Youth Innovation Team and Startup Funds from Qingdao University of Science and Technology.

Declaration of competing interest

The authors have no competing interests to declare that are relevant to the content of this article.

Author contribution statement

The manuscript was written through contributions of all authors.

References

[1] Chakraborty, I.; Pradeep, T. Atomically precise clusters of noble metals: Emerging link between atoms and nanoparticles. *Chem. Rev.* **2017**, *117*, 8208–8271.

[2] Jin, R. C.; Zeng, C. J.; Zhou, M.; Chen, Y. X. Atomically precise colloidal metal nanoclusters and nanoparticles: Fundamentals and opportunities. *Chem. Rev.* **2016**, *116*, 10346–10413.

[3] Shi, J. Y.; Kumar Gupta, R.; Deng, Y. K.; Sun, D.; Wang, Z. Recent advances in the asymmetrical templation effect of polyoxometalate in silver clusters. *Polyoxometalates* **2022**, *1*, 9140010.

[4] Zhang, S. S.; Havenridge, S.; Zhang, C. K.; Wang, Z.; Feng, L.; Gao, Z. Y.; Aikens, C. M.; Tung, C. H.; Sun, D. Sulfide boosting near-unity photoluminescence quantum yield of silver nanocluster. *J. Am. Chem. Soc.* **2022**, *144*, 18305–18314.

[5] Kang, X.; Wang, S. X.; Zhu, M. Z. Observation of a new type of aggregation-induced emission in nanoclusters. *Chem. Sci.* **2018**, *9*, 3062–3068.

[6] Zhang, M. M.; Gao, K. K.; Dong, X. Y.; Si, Y. B.; Jia, T.; Han, Z.; Zang, S. Q.; Mak, T. C. W. Chiral hydride Cu_{18} clusters transform to superatomic $Cu_{15}Ag_4$ clusters: Circularly polarized luminescence lighting. *J. Am. Chem. Soc.* **2023**, *145*, 22310–22316.

[7] Man, R. W. Y.; Yi, H.; Malola, S.; Takano, S.; Tsukuda, T.; Häkkinen, H.; Nambo, M.; Crudden, C. M. Synthesis and characterization of enantiopure chiral bis NHC-stabilized edge-shared Au_{10} nanocluster with unique prolate shape. *J. Am. Chem. Soc.* **2022**, *144*, 2056–2061.

[8] Ding, M.; Tang, L.; Ma, X. S.; Song, C. X.; Wang, S. X. Effects of ligand tuning and core doping of atomically precise copper nanoclusters on CO_2 electroreduction selectivity. *Commun. Chem.* **2022**, *5*, 172.

[9] Ma, G. Y.; Sun, F.; Qiao, L.; Shen, Q. L.; Wang, L.; Tang, Q.; Tang, Z. H. Atomically precise alkynyl-protected $Ag_{20}Cu_{12}$ nanocluster: Structure analysis and electrocatalytic performance toward nitrate reduction for NH_3 synthesis. *Nano Res.* **2023**, *16*, 10867–10872.

[10] Song, T. X.; Yao, Z.; Li, G. J.; Cai, X.; Liu, X.; Wang, Y. G.; Ding, W. P.; Zhu, Y. Catalytic activity coupled with structural stability within a heterodimeric $Au_{29}(SR)_{19}$ cluster. *ACS Catal.* **2023**, *13*, 10878–10886.

[11] Li, G. J.; Hou, J.; Lei, X. M.; Li, D.; Yu, E. Q.; Hu, W. G.; Cai, X.; Liu, X.; Chen, M. Y.; Zhu, Y. Reactivity and recyclability of ligand-protected metal cluster catalysts for CO_2 transformation. *Angew. Chem., Int. Ed.* **2023**, *62*, e202216735.

[12] Kwak, K.; Lee, D. Electrochemistry of atomically precise metal nanoclusters. *Acc. Chem. Res.* **2019**, *52*, 12–22.

[13] Tang, Q.; Lee, Y.; Li, D. Y.; Choi, W.; Liu, C. W.; Lee, D.; Jiang, D. E. Lattice-hydride mechanism in electrocatalytic CO_2 reduction by structurally precise copper-hydride nanoclusters. *J. Am. Chem. Soc.* **2017**, *139*, 9728–9736.

[14] Liu, Z. H.; Wu, Z. N.; Yao, Q. F.; Cao, Y. T.; Chai, O. J. H.; Xie, J. P. Correlations between the fundamentals and applications of ultrasmall metal nanoclusters: Recent advances in catalysis and biomedical applications. *Nano Today* **2021**, *36*, 101053.

[15] Wu, Z. L.; Hu, G. X.; Jiang, D. E.; Mullins, D. R.; Zhang, Q. F.; Allard, L. F.; Wang, L. S.; Overbury, S. H. Diphosphine-protected Au_{22} nanoclusters on oxide supports are active for gas-phase catalysis without ligand removal. *Nano Lett.* **2016**, *16*, 6560–6567.

[16] Wan, X. K.; Wang, J. Q.; Nan, Z. A.; Wang, Q. M. Ligand effects in catalysis by atomically precise gold nanoclusters. *Sci. Adv.* **2017**, *3*, e1701823.

[17] Kwak, K.; Choi, W.; Tang, Q.; Kim, M.; Lee, Y.; Jiang, D. E.; Lee, D. A molecule-like $PtAu_{24}(SC_6H_{13})_{18}$ nanocluster as an electrocatalyst for hydrogen production. *Nat. Commun.* **2017**, *8*, 14723.

[18] Sugiuchi, M.; Shichibu, Y.; Konishi, K. An Inherently chiral Au_{24} framework with double-helical hexagold strands. *Angew. Chem., Int. Ed.* **2018**, *57*, 7855–7859.

[19] Desireddy, A.; Conn, B. E.; Guo, J. S.; Yoon, B.; Barnett, R. N.; Monahan, B. M.; Kirschbaum, K.; Griffith, W. P.; Whetten, R. L.; Landman, U. et al. Ultrastable silver nanoparticles. *Nature* **2013**, *501*, 399–402.

[20] Liu, X.; Yuan, J. Y.; Yao, C. H.; Chen, J. S.; Li, L. L.; Bao, X. L.; Yang, J. L.; Wu, Z. K. Crystal and solution photoluminescence of $MAg_{24}(SR)_{18}$ (M = Ag/Pd/Pt/Au) nanoclusters and some implications for the photoluminescence mechanisms. *J. Phys. Chem. C* **2017**, *121*, 13848–13853.

[21] Liu, Y. J.; Shao, P.; Gao, M. Y.; Fang, W. H.; Zhang, J. Synthesis of Ag-doped polyoxotitanium nanoclusters for efficient electrocatalytic CO_2 reduction. *Inorg. Chem.* **2020**, *59*, 11442–11448.

[22] Zhai, Y. J.; Han, P.; Yun, Q. B.; Ge, Y. Y.; Zhang, X.; Chen, Y.; Zhang, H. Phase engineering of metal nanocatalysts for electrochemical CO_2 reduction. *eScience* **2022**, *2*, 467–485.

[23] Wang, Z.; Li, M. D.; Shi, J. Y.; Su, H. F.; Liu, J. W.; Feng, L.; Gao, Z. Y.; Xue, Q. W.; Tung, C. H.; Sun, D. et al. *In situ* capture of a ternary supramolecular cluster in a 58-nuclei silver supertetrahedron. *CCS Chem.* **2022**, *4*, 1788–1795.

[24] Su, Y. M.; Ji, B. Q.; Wang, Z.; Zhang, S. S.; Feng, L.; Gao, Z. Y.; Li, Y. W.; Tung, C. H.; Sun, D.; Zheng, L. S. Anionic passivation layer-assisted trapping of an icosahedral Ag_{13} kernel in a truncated tetrahedral Ag_{89} nanocluster. *Sci. China Chem.* **2021**, *64*, 1482–1486.

[25] Wang, Z.; Qu, Q. P.; Su, H. F.; Huang, P.; Gupta, R. K.; Liu, Q. Y.; Tung, C. H.; Sun, D.; Zheng, L. S. A novel 58-nuclei silver nanowheel encapsulating a subvalent Ag_6^{4+} kernel. *Sci. China Chem.* **2020**, *63*, 16–20.

[26] Yuan, Q. Q.; Kang, X.; Hu, D. Q.; Qin, C. W. L.; Wang, S. X.; Zhu, M. Z. Metal synergistic effect on cluster optical properties: Based on Ag_{25} series nanoclusters. *Dalton Trans.* **2019**, *48*, 13190–13196.

[27] Ma, X. H.; Jia, J. T.; Luo, P.; Wang, Z. Y.; Zang, S. Q.; Mak, T. C. W. Layer-by-layer alloying of NIR-II emissive M_{50} (Au/Ag/Cu) superatomic nanocluster. *Nano Res.* **2022**, *15*, 5569–5574.

[28] Bootharaju, M. S.; Joshi, C. P.; Parida, M. R.; Mohammed, O. F.; Bakr, O. M. Templated atom-precise galvanic synthesis and structure elucidation of a $[Ag_{24}Au(SR)_{18}]^-$ nanocluster. *Angew. Chem., Int. Ed.* **2016**, *55*, 922–926.

[29] Li, Q.; Lambright, K. J.; Taylor, M. G.; Kirschbaum, K.; Luo, T. Y.; Zhao, J. B.; Mpourmpakis, G.; Mokashi-Punekar, S.; Rosi, N. L.; Jin, R. C. Reconstructing the surface of gold nanoclusters by cadmium doping. *J. Am. Chem. Soc.* **2017**, *139*, 17779–17782.

[30] Yang, H. Y.; Wang, Y.; Huang, H. Q.; Gell, L.; Lehtovaara, L.; Malola, S.; Häkkinen, H.; Zheng, N. F. All-thiol-stabilized Ag_{44} and $Au_{12}Ag_{32}$ nanoparticles with single-crystal structures. *Nat. Commun.* **2013**, *4*, 2422.

[31] Kang, X.; Abroshan, H.; Wang, S. X.; Zhu, M. Z. Free valence electron centralization strategy for preparing ultrastable nanoclusters and their catalytic application. *Inorg. Chem.* **2019**, *58*, 11000–11009.

[32] Shen, H.; Xu, Z.; Wang, L. Z.; Han, Y. Z.; Liu, X. H.; Malola, S.; Teo, B. K.; Häkkinen, H.; Zheng, N. F. Tertiary chiral nanostructures from C-H ⋯ F directed assembly of chiroptical superatoms. *Angew. Chem., Int. Ed.* **2021**, *60*, 22411–22416.

[33] Li, H.; Zhou, C. J.; Wang, E. D.; Kang, X.; Xu, W. W.; Zhu, M. Z. An insight, at the atomic level, into the intramolecular metallophilic interaction in nanoclusters. *Chem. Commun.* **2022**, *58*, 5092–5095.

[34] Anumula, R.; Reber, A. C.; An, P.; Cui, C. N.; Guo, M. D.; Wu, H. M.; Luo, Z. X.; Khanna, S. N. Ligand accommodation causes the anti-centrosymmetric structure of $Au_{13}Cu_4$ clusters with near-infrared emission. *Nanoscale* **2020**, *12*, 14801–14807.

[35] Wang, J. Q.; He, R. L.; Liu, W. D.; Feng, Q. Y.; Zhang, Y. E.; Liu, C. Y.; Ge, J. X.; Wang, Q. M. Integration of metal catalysis and organocatalysis in a metal nanocluster with anchored proline. *J. Am. Chem. Soc.* **2023**, *145*, 12255–12263.

[36] Zhang, S. S.; Liu, R. C.; Zhang, X. C.; Feng, L.; Xue, Q. W.; Gao, Z. Y.; Tung, C. H.; Sun, D. Core engineering of paired core-shell silver nanoclusters. *Sci. China Chem.* **2021**, *64*, 2118–2124.

[37] Wang, Z.; Su, H. F.; Zhuang, G. L.; Kurmoo, M.; Tung, C. H.; Sun, D.; Zheng, L. S. Carbonate-water supramolecule trapped in silver nanoclusters encapsulating unprecedented Ag_{11} Kernel. *CCS Chem.* **2020**, *2*, 663–672.

[38] Rambukwella, M.; Chang, L.; Ravishanker, A.; Fortunelli, A.; Stener, M.; Dass, A. $Au_{36}(SePh)_{24}$ nanomolecules: Synthesis, optical spectroscopy and theoretical analysis. *Phys. Chem. Chem. Phys.* **2018**, *20*, 13255–13262.

[39] Zeng, C. J.; Qian, H. F.; Li, T.; Li, G.; Rosi, N. L.; Yoon, B.; Barnett, R. N.; Whetten, R. L.; Landman, U.; Jin, R. C. Total structure and electronic properties of the gold nanocrystal $Au_{36}(SR)_{24}$. *Angew. Chem., Int. Ed.* **2012**, *51*, 13114–13118.

[40] Ma, A. L.; Wang, J. W.; Kong, J.; Ren, Y. G.; Wang, Y. X.; Ma, X. S.; Zhou, M.; Wang, S. X. $Au_{10}Ag_{17}(TPP)_{10}(SR)_6Cl_5$ nanocluster: Structure, transformation and the origin of its photoluminescence. *Phys. Chem. Chem. Phys.* **2023**, *25*, 9772–9778.

[41] Klementyeva, S. V.; Woern, K.; Schrenk, C.; Zhang, M. H.; Khusniyarov, M. M.; Schnepf, A. $[(thf)_5Ln(Ge_9\{Si(SiMe_3)_3\}_2)]$ (Ln = Eu, Sm, Yb): Capping metalloid germanium cluster with lanthanides. *Inorg. Chem.* **2023**, *62*, 5614–5621.

[42] Luo, Z. T.; Yuan, X.; Yu, Y.; Zhang, Q. B.; Leong, D. T.; Lee, J. Y.; Xie, J. P. From aggregation-induced emission of Au(I)-thiolate complexes to ultrabright Au(0)@Au(I)-thiolate core-shell nanoclusters. *J. Am. Chem. Soc.* **2012**, *134*, 16662–16670.

[43] Wu, Z. K.; Jin, R. C. On the ligand's role in the fluorescence of gold nanoclusters. *Nano Lett.* **2010**, *10*, 2568–2573.

[44] Sun, Y. N.; Liu, X.; Xiao, K.; Zhu, Y.; Chen, M. Y. Active-site tailoring of gold cluster catalysts for electrochemical CO_2 reduction. *ACS Catal.* **2021**, *11*, 11551–11560.

[45] Seong, H.; Efremov, V.; Park, G.; Kim, H.; Yoo, J. S.; Lee, D. Atomically precise gold nanoclusters as model catalysts for identifying active sites for electroreduction of CO_2. *Angew. Chem., Int. Ed.* **2021**, *60*, 14563–14570.

[46] Deng, G. C.; Kim, J.; Bootharaju, M. S.; Sun, F.; Lee, K.; Tang, Q.; Hwang, Y. J.; Hyeon, T. Body-centered-cubic-kernelled $Ag_{15}Cu_6$ nanocluster with alkynyl protection: Synthesis, total Structure, and CO_2 electroreduction. *J. Am. Chem. Soc.* **2022**, *145*, 3401–3407.

[47] Zang, D. J.; Li, Q.; Dai, G. Y.; Zeng, M. Y.; Huang, Y. C.; Wei, Y. G. Interface engineering of Mo_8/Cu heterostructures toward highly selective electrochemical reduction of carbon dioxide into acetate. *Appl. Catal. B Environ.* **2021**, *281*, 119426.

[48] Liu, L. H.; Li, N.; Han, M.; Han, J. R.; Liang, H. Y. Scalable synthesis of nanoporous high entropy alloys for electrocatalytic oxygen evolution. *Rare Met.* **2022**, *41*, 125–131.

[49] Cai, Y. F.; Fei, C.; Zhang, C.; Yang, J.; Wang, L.; Zhan, W. C.; Guo, Y. L.; Cao, X. M.; Gong, X. Q.; Guo, Y. Surface pits stabilized Au catalyst for low-temperature CO oxidation. *Rare Met.* **2022**, *41*, 3060–3068.

[50] Qin, L. B.; Sun, F.; Ma, X. S.; Ma, G. Y.; Tang, Y.; Wang, L. K.; Tang, Q.; Jin, R. C.; Tang, Z. H. Homoleptic alkynyl-protected Ag_{15} nanocluster with atomic precision: Structural analysis and electrocatalytic performance toward CO_2 reduction. *Angew. Chem., Int. Ed.* **2021**, *60*, 26136–26141.

[51] Li, Q. Z.; Huang, B. Y.; Yang, S.; Zhang, H.; Chai, J. S.; Pei, Y.; Zhu, M. Z. Unraveling the nucleation process from a Au(I)-SR complex to transition-size nanoclusters. *J. Am. Chem. Soc.* **2021**, *143*,

15224–15232.
[52] Ma, X. S.; Sun, F.; Qin, L. B.; Liu, Y. G.; Kang, X. W.; Wang, L. K.; Jiang, D. E.; Tang, Q.; Tang, Z. H. Electrochemical CO_2 reduction catalyzed by atomically precise alkynyl-protected Au_7Ag_8, Ag_9Cu_6, and $Au_2Ag_8Cu_5$ nanoclusters: Probing the effect of multi-metal core on selectivity. *Chem. Sci.* **2022**, *13*, 10149–10158.
[53] Wang, K.; Liu, D. Y.; Liu, L. M.; Liu, J.; Hu, X. F.; Li, P.; Li, M. T.; Vasenko, A. S.; Xiao, C. H.; Ding, S. J. Tuning the local electronic structure of oxygen vacancies over copper-doped zinc oxide for efficient CO_2 electroreduction. *eScience.* **2022**, *2*, 518–528.

Along Ma received his B.S. degree from Anhui Agricultural University in 2020 and M.S. degree from Qingdao University of Science and Technology in 2023. He is currently a research assistant in the College of Materials Science and Engineering, Qingdao University of Science and Technology. His research interests include the design and synthesis of silver-based nanoclusters, as well as their related properties in photoluminescence and electrocatalytic CO_2 reduction reaction.

Jiawei Wang received his B.S. degree from Anhui Agricultural University in 2021. Currently, he is pursuing a master's degree in the College of Materials Science and Engineering, Qingdao University of Science and Technology. His research interests include the synthesis of gold-silver alloy nanoclusters and related properties in photoluminescence and electrocatalytic CO_2 reduction reaction.

Yifei Wang is studying for a B.S. degree in the College of Materials Science and Engineering, Qingdao University of Science and Technology. Her main research interests are related to the synthesis of gold-silver alloy nanoclusters.

Zuo Yang received his B.E. degree from Qingdao University of Science and Technology in 2023. Currently, he is pursuing a master's degree in the College of Materials Science and Engineering at Qingdao University of Science and Technology. His research interests include the synthesis of metal nanoclusters and their electrocatalytic properties in CO2 reduction.

Yonggang Ren received his B.S. degree from China University of Petroleum (East China) in 2022. Currently, he is pursuing a master's degree in the College of Materials Science and Engineering, Qingdao University of Science and Technology. His research interests include the synthesis of silver-based nanoclusters and their properties in photoluminescence and electrocatalytic CO2 reduction reaction.

Xiaoshuang Ma received his B.E. degree from Shandong Institute of Petroleum and Chemical Technology in 2014, M.S. degree from Qilu University of Technology in 2017 and Ph.D. degree from South China University of Technology in 2021 under the guidance of Prof. Zhenghua Tang. He is currently an associate professor in the College of Materials Science and Engineering, Qingdao University of Science and Technology. His research interests include the design and synthesis of copper-based nanoclusters, as well as electrochemical CO2RR.

Shuxin Wang received his B.S. degree in 2008, M.S. degree in 2012 and Ph.D. degree in 2016 under the guidance of Prof. Manzhou Zhu from Anhui University. As a joint Ph.D. student, he studied at Carnegie Mellon University under the Guidance of Prof. Rongchao Jin between 2014 and 2016. Further, he worked as a research professor at Anhui University from 2016 to 2019. In 2020, he joined the College of Materials Science and Engineering, Qingdao University of Science and Technology. His research concerns the controlled synthesis and structure-property relationships of alloy nanoclusters, as well as machine learning.